



LAWRENCE  
LIVERMORE  
NATIONAL  
LABORATORY

LLNL-JRNL-667679

# THE SCALING OF ELECTRON AND POSITRON GENERATION IN INTENSE LASER-SOLID INTERACTIONS

H. Chen, A. Link, Y. Sentoku, P. Audebert, F. Fiuzal, A. Hazi,  
R. F. Hetter, M. Hill, L. Hobbs, A. J. Kemp, G. E. Kemp, S.  
Kerr, D. D. Meyerhofer, J. Myatt, S. R. Nagel, J. Park, R.  
Tommasini, G. J. Williams

February 23, 2015

Physics of Plasmas

## **Disclaimer**

---

This document was prepared as an account of work sponsored by an agency of the United States government. Neither the United States government nor Lawrence Livermore National Security, LLC, nor any of their employees makes any warranty, expressed or implied, or assumes any legal liability or responsibility for the accuracy, completeness, or usefulness of any information, apparatus, product, or process disclosed, or represents that its use would not infringe privately owned rights. Reference herein to any specific commercial product, process, or service by trade name, trademark, manufacturer, or otherwise does not necessarily constitute or imply its endorsement, recommendation, or favoring by the United States government or Lawrence Livermore National Security, LLC. The views and opinions of authors expressed herein do not necessarily state or reflect those of the United States government or Lawrence Livermore National Security, LLC, and shall not be used for advertising or product endorsement purposes.

# THE SCALING OF ELECTRON AND POSITRON GENERATION IN INTENSE LASER-SOLID INTERACTIONS

Hui Chen<sup>1</sup>, A. Link<sup>1</sup>, Y. Sentoku<sup>2</sup>, P. Audebert<sup>3</sup>, F. Fiuza<sup>1</sup>, A. Hazi<sup>1</sup>, R. F. Heeter<sup>1</sup>, M. Hill<sup>4</sup>, L. Hobbs<sup>4</sup>, A. J. Kemp<sup>1</sup>, G. E. Kemp<sup>1</sup>, S. Kerr<sup>5</sup>, D. D. Meyerhofer<sup>6</sup>, J. Myatt<sup>6</sup>, S. R. Nagel<sup>1</sup>, J. Park<sup>1</sup>, R. Tommasini<sup>1</sup>, G. J. Williams<sup>1</sup>,

1. Lawrence Livermore National Laboratory, California 94550, USA
2. University of Nevada, Reno, Nevada 89557, USA
3. LULI, École Polytechnique, Palaiseau 91128, France
4. Directorate of Science and Technology, AWE plc, Reading RG7 4PR, UK
5. University of Alberta, Alberta T6G 2R3, Canada
6. LLE, University of Rochester, Rochester, New York 14623, USA

## Abstract:

This paper presents experimental scalings of the electrons and positrons produced by intense laser-target interactions at relativistic laser intensities ( $10^{18} - 10^{20} \text{ Wcm}^{-2}$ ). The data were acquired from three short-pulse laser facilities with laser energies ranging from 80 – 1500 J. We found a non-linear ( $\approx E_L^2$ ) scaling of positron yield<sup>1</sup> and a linear scaling of electron yield with the laser energy. These scalings are explained by theoretical and numerical analyses. Positron acceleration by the target sheath field is confirmed by the positron energy spectrum, which has a pronounced peak at energies near the sheath potential, as determined by the observed maximum energies of accelerated protons. The parameters of laser-produced electron-positron jets are summarized together with the

theoretical energy scaling. The measured energy-squared scaling of relativistic electron-positron jets indicates the possibility to create an astrophysically relevant experimental platform with such jets using multi-kilojoule high intensity lasers currently under construction.

PACS numbers: 52.38.-r; 52.38.Ph; 52.59.-f

## I. INTRODUCTION

It has been suggested<sup>2</sup> that laboratory experiments may one day help to understand the physics of relativistic shocks in extreme astrophysical environments, such as Gamma Ray Bursts (GRBs), Active Galactic Nuclei (AGN), Black Holes and Pulsar Wind Nebulae (PWN).<sup>3-11</sup> This perspective has motivated worldwide efforts to generate high-flux and high-energy electron-positron “pair” jets, aiming to replicate the physics of GRBs in the laboratory<sup>1</sup>. To date such efforts remain incomplete.

In the non-relativistic regime, positrons and positron plasmas from radioactive isotopes or accelerators are studied extensively in areas related to basic antimatter science, such as antihydrogen experiments<sup>12,13</sup> and Bose-Einstein condensation of positronium.<sup>14,15</sup> In the relativistic regime, making an astrophysically relevant pair plasma jet is challenging due to the difficulties associated with achieving the required densities and relativistic energies within the short lifetime of a positron. However, rapid progress has been made over the past few years in using intense short laser pulses to drive mm-thick high-Z (gold) targets and produce large numbers of positrons.<sup>10</sup> Since the first experiment in 1999,<sup>16</sup> the positron yield per laser pulse has increased by several orders of magnitude. It was found that laser-produced positrons have several characteristics that may prove

essential for developing an astrophysically relevant platform. The first is that intense lasers can make a very large number of positrons ( $10^{10}$  to  $10^{12}$  per shot) in a short time (1 – 100 ps). This feature, in combination with the small volume ( $\sim \text{mm}^3$ ) these positrons occupy “at birth”, implies a high positron density, at least for a short time. The second characteristic is that the electrons escaping from the high-Z target produce an electric field, aligned with the target surface normal, which accelerates the positrons leaving the target to a few tens of MeV. This means that a dense burst of positrons can be born and accelerated to relativistic velocities in an integrated process. The third characteristic is that the MeV electrons and positrons produced from the laser-target interaction form overlapping jets behind the target, allowing much higher pair density to be achieved than would be possible if the particle velocities were distributed isotropically.

So far, positron densities of  $10^{12}$  -  $10^{13} \text{ cm}^{-3}$  at the source have been achieved.<sup>17</sup> For interacting electron-positron jets to initiate the astrophysically interesting electromagnetic instabilities, the electron-positron density needs to be  $10^{14}$  -  $10^{16} \text{ cm}^{-3}$ ,<sup>1</sup> 2-4 orders of magnitude more than that demonstrated to date. To increase the pair density, one can either (1) increase the number of particles, or (2) reduce the volume of the particles, or both. The laser spot diameter sets a fundamental limit on the intrinsic volume where the pairs are generated. An additional constraint is posed by the finite target thickness ( $\sim 1$  mm) required to efficiently produce positrons via the Bethe-Heitler process. The density of the interacting pair jet can be increased through collimation or confinement of the pairs using external magnetic fields.<sup>18,19</sup> However, for relativistic pairs the required field strength is quite high, a few hundreds of Tesla, making the configuration challenging.

Therefore, it is essential to increase the pair yield to be able to observe instability growth in the interaction of these short duration laser-produced pair jets.

To increase the pair yield, it is important to understand the electron scaling with laser parameters. This is due to the indirect nature of pair production with intense lasers through the Bethe-Heitler (B-H) process.<sup>20</sup> The laser first accelerates electrons to relativistic energies through a laser-plasma interaction, which takes place either in the underdense plasma on the front side of the solid target, or at the overdense surface of a solid target. (The laser wake-field electron acceleration approach for positron production has been addressed elsewhere<sup>21</sup> and is outside the scope of this paper). The scattering of these relativistic electrons with a high density, high atomic number target produces high-energy (MeV) photons via bremsstrahlung (so called  $\gamma$ -rays), which decay and produce pairs in the field of the target nuclei via the B-H process.

This paper reports extensive experimental results for electrons and positrons obtained at three different laser facilities. These data establish the scaling of electrons and positrons as a function of laser energy for a large range of laser parameters (70 – 1500 J, 1-10 ps and  $10^{18} - 10^{20}$  Wcm<sup>-2</sup>). The data reveals much of the physics behind the scaling of pair yield, positron acceleration, and angular divergence. The observed yield scaling indicates that with  $\sim 10$  kJ of laser energy, one might be able to produce astrophysically relevant pair jets in the laboratory.

The paper is organized as follows. Section II describes the laser parameters, experimental setup and diagnostics. Section III discusses the electron scaling as function of laser energy/intensity. Section IV presents the scaling of positron number, acceleration and angular divergences. Section V summarizes the parameters of the pair jets relative to

the requirement for laboratory astrophysics studies. Section VI concludes the paper with a brief discussion for future development.

## II. Experimental setup

The experiments were performed over  $\sim 5$  years on 3 facilities: the Titan laser<sup>22</sup> at Lawrence Livermore National Laboratory, the Omega-EP laser<sup>23</sup> of the Laboratory for Laser Energetics at the University of Rochester, and the Orion laser<sup>24</sup> at AWE in the UK. The experimental conditions were controlled as close as possible to compare the results from each facility. For this study, data from 54 target shots (23 from Omega EP, 7 from Orion, and the 24 from Titan) are presented and compared in terms of the laser, target, and diagnostic parameters.

All three lasers have a wavelength of  $1.054 \mu\text{m}$  and an off-axis-parabola ( $f/2$  or  $f/3$ ) as the final focusing optic. The data presented were obtained with the best laser-contrast available, without using an auxiliary laser pulse to create a pre-formed plasma in front of the target. The laser parameters are listed in Table 1.

Table 1: Laser parameters used in the experiments for this paper.

	Pulse Length (ps)	Focal Spot ( $\mu\text{m}$ )	Energy (J)	Laser Intensity ( $\text{W}/\text{cm}^2$ )	Contrast in laser intensity
<b>Titan</b>	0.7	8-15	50-150	$\sim 10^{19} - 10^{20}$	$>10^6$
	10	8-15	100 - 350	$\sim 10^{18} - 10^{19}$	$>10^6$
<b>Omega EP</b>	10	25-50	100 - 1500	$\sim 10^{18} - 10^{19}$	$>10^7$
<b>Orion</b>	0.7	$\sim 15$	100 - 500	$\sim 10^{19} - 10^{20}$	$>10^6$

A typical experimental setup is shown in Fig. 1. All targets were identical gold discs 1 mm thick and 2 mm in diameter. Laser incidence on the target was at an angle (relative to the target normal) of 0, 15, and 18 degrees for Omega EP, Orion, and Titan, respectively. The small variation in laser incident angle was found to have a negligible effect on the laser-electron conversion.

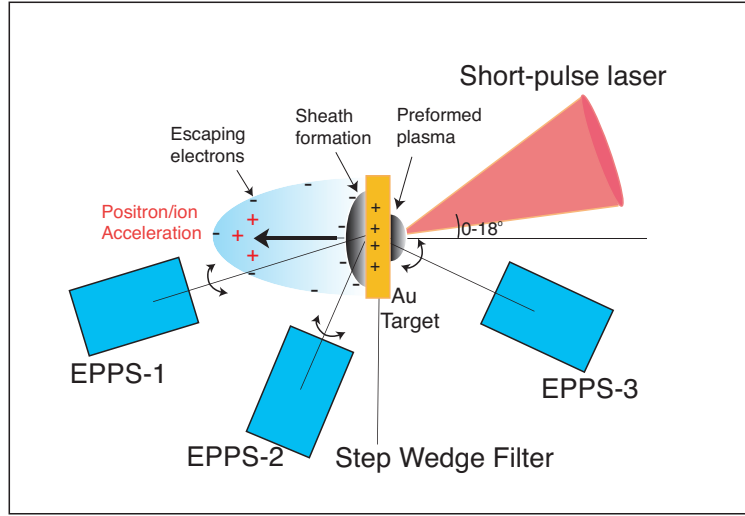


*Figure 1: Illustration of experimental setup at Titan. A similar setup was used on the Omega EP and Orion experiments, but with slightly different laser incidence angles and diagnostic locations.*

The primary diagnostics included several Electron-Positron-Proton Spectrometers (EPPS)<sup>25</sup> and a step wedge filter pack.<sup>26</sup> The step wedge filter packs used on Omega EP measured the high-energy bremsstrahlung photons between 0.1 and 1 MeV, from which the relative high-energy photon yield was derived.

Up to three EPPS were used on the Titan experiments at various angles (see Fig. 1) while two were used on the Omega EP (one normal, and another parallel to the rear surface of the target). Only one EPPS (along the laser's propagation direction) was used at Orion, due to space limitations. With the EPPS diagnostics, the energy spectra of



electrons, positrons, and protons were simultaneously measured for each shot. In these experiments the solid angle (entrance aperture and location) of the spectrometer was optimized to obtain good positron signals, which are lower than the electron and proton signals. Consequently, the proton signal was often saturated at the peak of the distribution, but the maximum proton energy was recorded on most shots. Sample raw data images from EPPS are shown in Fig. 2 (top), where the signals from the respective sources are marked. The glow outside the signal strip was from the hard x-ray background, which was subtracted to obtain the reported signals.<sup>9</sup> For a number of shots (in Titan and Orion experiments) the electron data were not available due to operational errors.

Samples of absolutely calibrated electron and positron spectra measured for three Omega EP shots are shown in Fig. 2 (bottom). The laser energies were 250 J, 800 J and 1500 J, with similar laser focal spots and 10 ps pulse durations. From the EPPS spectra, one can obtain (A) escaped hot electron temperature, (B) the total number and energy of escaped electrons and positrons, (C) the positron acceleration and (D) the maximum proton energy (not shown). While it is straightforward to obtain (C) and (D) from the measured spectra, additional considerations are needed to determine (A) and (B).

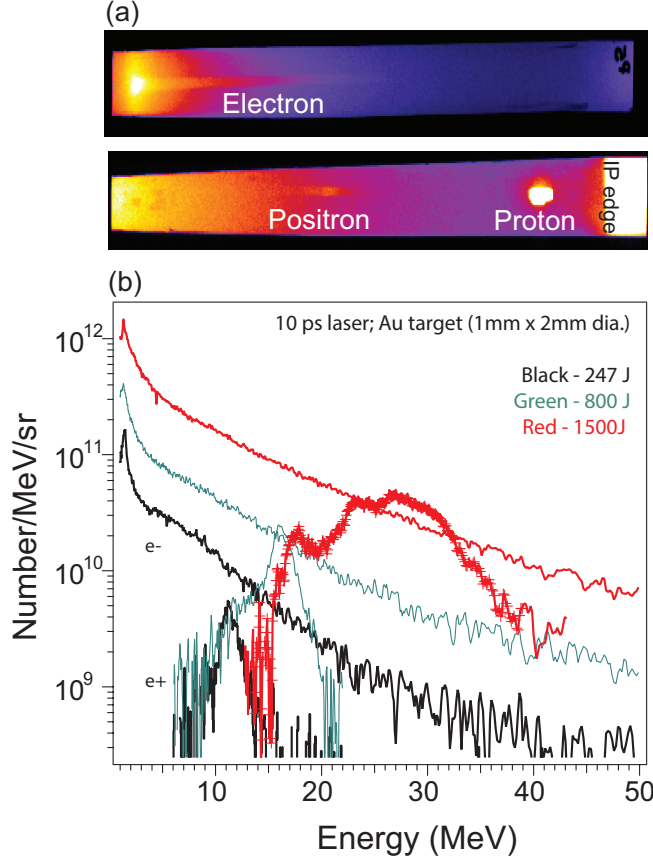


Figure 2 (a): The raw images from EPPS for positive particles (protons and positrons) and electrons for laser energy at 800 J; (b): Three pairs of electron and positron energy spectra for laser energy of 247 J, 800 J and 1500 J from the EPPS measurements.

(A) The hot electron temperatures were obtained by fitting the electron spectra with an exponential function  $\sim e^{-E/T_e}$ , where  $E$  is the electron kinetic energy, and  $T_e$  is the “hot electron temperature”. As MeV electrons are important to positron production, we analyzed their spectra from 5 MeV to the maximum detected electron energy. Below 5 MeV, the electron data are strongly influenced by the  $\sim \text{MV}/\mu\text{m}$ -scale electric field present at the vacuum-target interface,<sup>27</sup> and it is often difficult to describe the measured spectrum with  $T_e$  (see Appendix-1). At energies  $>5$  MeV, the measured escaping

electrons reflect the distribution of laser-accelerated electrons with reasonable accuracy according to the simulations done with the hybrid particle-in-cell (PIC) code LSP.<sup>27</sup> Independent 2D PIC simulations using code PSC<sup>28</sup> arrived the same conclusion. The result of PSC simulation is illustrated in Fig. 3: while there are significant differences in electron distributions between the source and escaping electrons at electron energies less than  $\sim 5$  MeV, the slope of the distributions ( $T_e$ ) at higher electron energies are very similar for both.

$T_e$  is useful not only as an input parameter for the analytical and Monte-Carlo calculations of positron production (see Section IV), but also to understand the dominant laser-plasma interaction mechanism.<sup>29,30</sup>

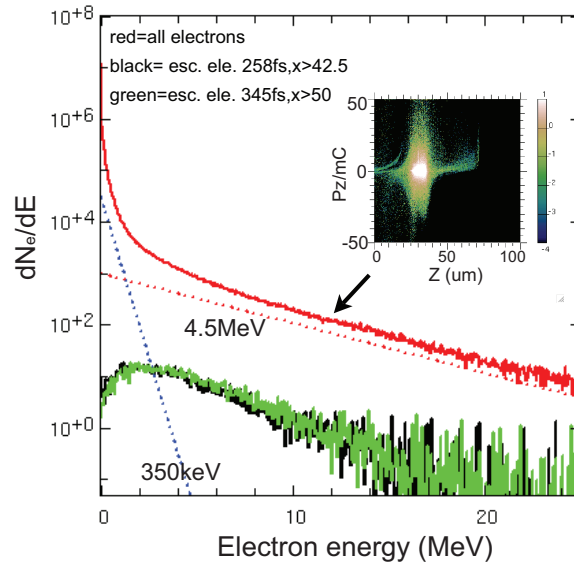


Figure 3: 2D PSC PIC simulation results of the electron distribution from laser-plasma interaction (red) comparing to the escaping electron distribution (green). The dashed lines are exponential fits of the source distribution using temperatures of 350 keV and 4.5 MeV.

(B) To calculate the total number of electrons and positrons, one needs to take into account angular information, since strongly anisotropic distributions were observed for both species.<sup>18,17</sup> While the angular distributions from Titan and Omega EP were measured,<sup>19</sup> the angular profile on Orion was extrapolated from the Titan and Omega EP data as having a full width at half-maximum of less than 30 degrees.

The uncertainty in the measured positron yield comes from several aspects of the measurements (angular distribution  $\sim 20\%$ , spectrometer calibration  $\sim 20\%$ , image plate read-out  $\sim 15\%$ ), bringing the total error to about 30% for each data point. For the laser intensities associated with each data point, the total uncertainty (30%-50%) comes from the uncertainties from laser energy measurement ( $\sim 5\%$ -10%), laser pulse length ( $\sim 10\%$ -20%), and focal spot size measurements (20%-40%). As will be seen later, there is appreciable scatter of the data, which is most likely due to differences in preformed plasma profiles resulting from shot-to-shot variation of the energy in the intrinsic laser prepulse [see Appendix-2]. Previous work<sup>31</sup> has shown that variations in pre-plasma scale-length can affect the fraction of absorbed laser energy and the resulting hot electron production.

### III. Electron production

The data shows the escaped electron temperature a function of laser energy in Fig. 4 and laser intensity in Fig. 5. For each data point, the intensity is calculated using the measured laser energy, the laser focal area containing 68% of the energy and the full-width-at-half-maximum laser pulse length for each shot. For some shots, it was not possible to fit the distribution with a single slope (see Appendix-1). An alternate description is given by the

total number and energy of the electrons obtained by integrated over the distribution. Their dependence on the laser energy and the intensity are also relatively weak.

The energy distribution of the electrons is sensitive to the temporal and spatial profiles of the laser pulse,<sup>31,32</sup> as well as the scale-length of the preformed plasma, electron-ion energy transfer and electron transport. For the same laser/target configuration, the most important parameter affecting the electron distribution is the plasma scale-length at the front surface of the target. It is well-known that different electron acceleration mechanisms operate in different regions of the plasma.<sup>33</sup> Near the critical density (defined as the density above which the laser does not propagate) acceleration occurs predominantly through the  $\mathbf{J} \times \mathbf{B}$  mechanism, leading to the so-called ponderomotive scaling<sup>29</sup> of  $T_e$  as a function of the local laser intensity,  $I$  (in  $\text{Wcm}^{-2}$ ):

$$T_e \approx 0.511 \times \left( \sqrt{1 + I \lambda^2 / 1.4 \times 10^{18}} - 1 \right) \text{ (MeV)}, \text{ where } \lambda \text{ is the laser wavelength in } \mu\text{m. In}$$

the under-dense region of the plasma, primarily produced via ablation from the laser pre-pulse, electron acceleration occurs due to stochastic processes<sup>31</sup> and  $T_e$  is given by<sup>30</sup>

$$T_e \approx 1.5 \times \left( \sqrt{I \lambda^2 / 10^{18}} \right) \text{ (MeV)} - \text{referred to as Pukhov scaling hereafter. These two}$$

mechanisms represent the limiting cases of the laser-plasma interaction conditions present in our experiments. The latter is responsible for the generation of the most energetic electrons and therefore is expected to play a dominant role in pair production. Recent simulations for similar laser and plasma conditions confirm that indeed the most energetic electrons originate in the underdense plasma region.<sup>31</sup>

A comparison to the experimental electron temperature results is shown in Fig. 5. Because of the dearth of electron temperature data at high laser intensity, we used a few

shots obtained from Omega EP on different sized gold targets at higher intensities. Using these data is reasonable in Fig. 5 because the electron temperature has, at most, a very weak dependence on the target size (see Appendix-3). Fig. 5 shows that the Pukhov scaling appears to fit the data better, supporting the hypothesis that acceleration in the under-dense plasma is dominant in our experiments.

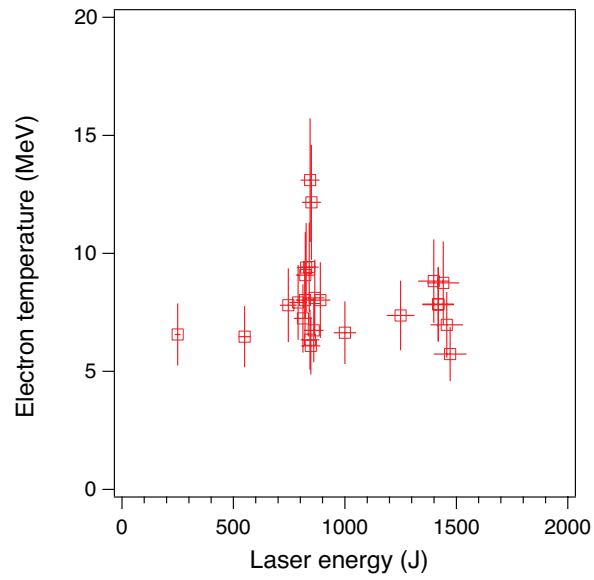


*Figure 4: Hot electron temperatures at various laser energies inferred from Omega EP data taken with a laser pulse of 10 ps.*

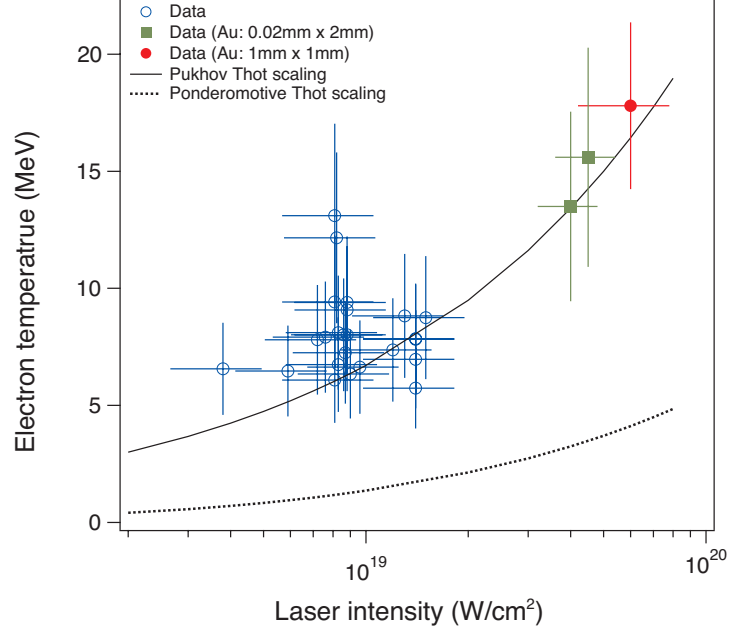


Figure 5: Hot electron temperature data (open circles) measured for the standard targets as a function of laser intensity. Data from higher intensities are shown for smaller target (filled circle) and thinner targets (squares). Also shown are the hot electron temperatures from the ponderomotive scaling (dotted line) and Pukhov scaling (solid line).

The electron energy distribution (described here with  $T_e$ ) is the critical input into a set of particle transport calculations of the bremsstrahlung generation and pair production by the Bethe-Heitler process (see Sec. IV). In this set of calculations, electrons, positrons, and photons that leave the target are counted using specific “diagnostics” defined by the actual experimental instrument’s line-of-sight, energy range, and solid angle, such that results can be directly compared with the experimental data.

For example, the calculated high-energy (0.1 – 1 MeV) bremsstrahlung yield is compared to that measured at Omega EP in Fig. 6: the increase in the photon yield with increasing laser intensity is well described by an analytic calculation (see Sec. IV) using the measured electron distribution. An absolute comparison of the bremsstrahlung yield

was not available because the spatial distribution of the radiation was not measured in the experiment. It should be noted that, although most pair production happens at photon energies  $> 1$  MeV, our diagnostic is sensitive to  $0.1 - 1$  MeV photons.<sup>26</sup> A comparison of theory and experiment in this energy range is useful to understand the intermediate step (electrons to photons) in the pair production and to confirm the yield calculations.

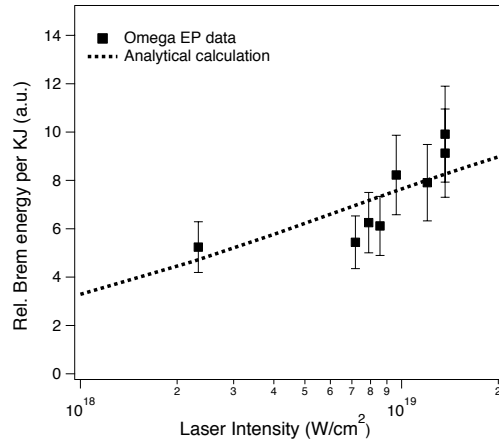


Figure 6: Relative bremsstrahlung energy per kJ laser energy as a function of laser intensity.

The total number of electrons can be deduced from the measured spectra and the angular distribution. The electron yield increases approximately linearly for data from laser energy higher than 500 J (Fig. 7). At lower laser energies, the data had too much scatters to provide a unique fit. The linear fit gives:  $N_e = 2.3(\pm 0.5) \times 10^9 E_L$ . This result is in stark contrast with the scaling obtained for positrons,<sup>1</sup> which will be discussed in the next section.



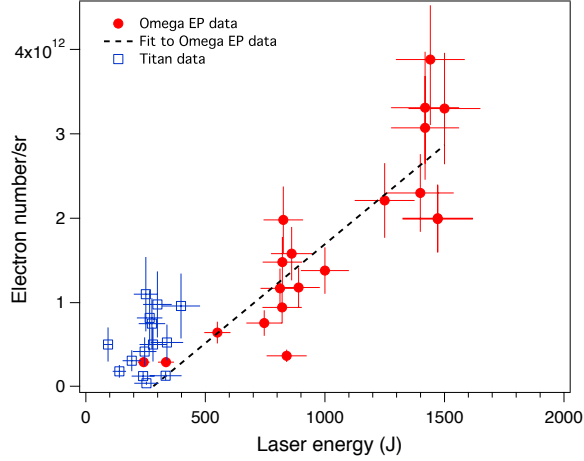


Figure 7: The total electron number as a function of laser energy (squares and circles with error bars) and the fit to the data (dashed line).

#### IV. Positron production

The positron data from the EPPS can be characterized in terms of the total yield, energy of the spectral peak and angular divergence. The scaling of these observables with laser parameters is presented below.

##### A Positron yield – experimental results

Figure 8 shows the positron yield as a function of the laser energy obtained from the three facilities. Assuming constant laser-electron conversion efficiency,<sup>34</sup> one might expect a linear dependence of the positron yield vs laser energy. However the data show that the dependence is better fitted with a near quadratic function.<sup>1</sup> The positron data points in Figure 8 fall into two groups. The upper group is from shots with  $\sim 1$  ps laser pulses at Titan (orange triangles) and Orion (green upside down triangles). The lower group is obtained with 10 ps laser pulses on Titan (blue triangles) and Omega EP (red circles). The lines show the best fits to the data in each group. As a function of laser energy  $E_L$  (in J) the fits give:  $N_{e^+} \sim 4(\pm 9) \times 10^5 E_L^{(2.3 \pm 0.4)}$  and  $N_{e^+} \sim 2(\pm 3) \times 10^5 E_L^{(2.0 \pm 0.3)}$  for 1 and 10 ps,

respectively. Both data groups show a non-linear, approximately quadratic dependence of the positron yield on the incident laser energy.

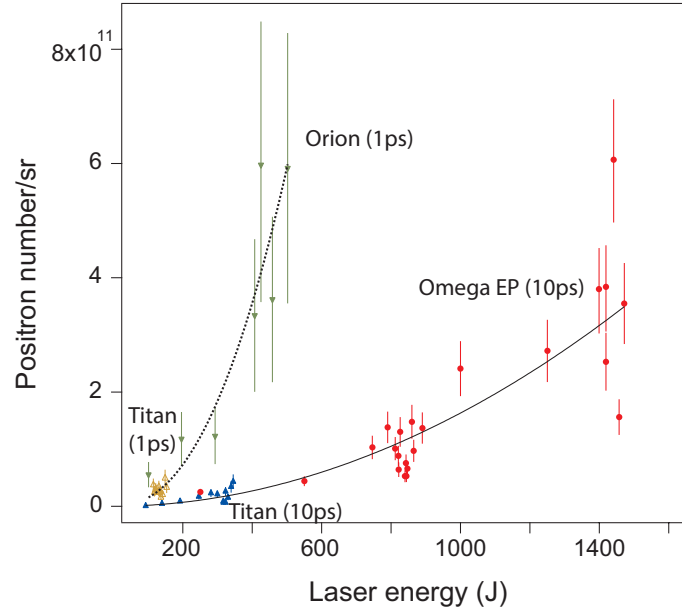


Figure 8: Positron number/sr as a function of laser energy from shots with 1 ps laser pulse: Titan (orange triangles) and Orion (green upside down triangles); and the data obtained with 10 ps laser pulse: Titan (blue triangles) and Omega EP (red dots) [data from Ref. 1].

The normalized positron yield per kJ laser energy as a function of laser intensity<sup>1</sup> is shown in Fig. 9. The normalized positron yield increases with laser intensity as  $N_{e^+}/\text{kJ} \sim I^{(1.2 \pm 0.1)}$ .

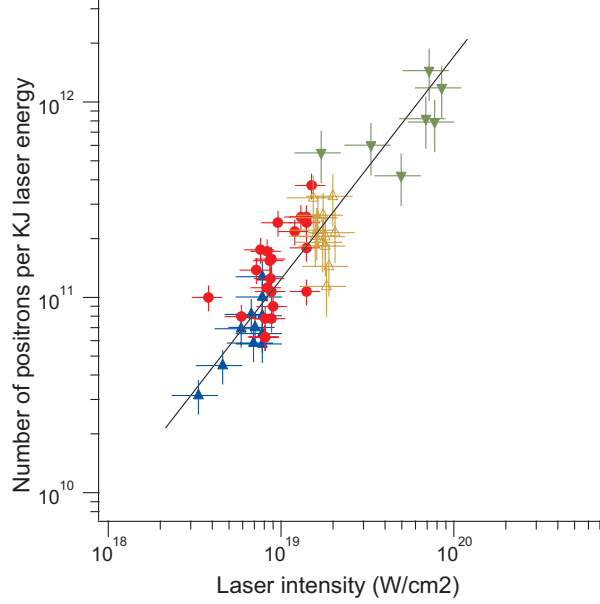


Figure 9: Positron yield per kJ laser energy as a function of laser intensity. Data include that from Titan (blue and open orange triangles), Orion (green upside down triangles); and Omega EP (red dots) [Data from Ref. 1].

## B Positron yield – Analytical calculations and simulations

To understand the scaling of the positrons, three computational approaches are applied: (I) analytical method, (II) GEANT4 Monte-Carlo simulation, and (III) LSP PIC simulations. For all three techniques, the normalized positron yield is calculated for direct comparison with the measurement. For the electron source, the first two methods assumed a Boltzmann distribution at  $T_e$ , which is related to the laser intensity through either ponderomotive or Pukhov scaling as described in Sec. III. In the LSP simulation, the electron source was self-generated by simulating the laser-plasma interaction. Since the first two methods start with the electron energy distribution, the laser-electron conversion efficiency has to be estimated. This was calculated by method (III) to be about 40%, and the same value was used for the analytic method and GEANT4. Another distinction between the methods is the ability to include electron refluxing; method (I)

used a simple factor; in method (III) LSP calculated it self-consistently, while it was not included in the GEANT4 (Method II). Below, we describe each method in more detail and compare the their predictions to the experimental data.

(I) The analytical calculations used the formula from Myatt, et al.<sup>35</sup> Briefly, the positron yield is  $Y_{e^+} = \int_0^\infty dk N_\gamma(k) \sigma_{\gamma \rightarrow e^+e^-}(k) dk \langle \rho L \rangle_\Omega$  – where variable  $k$  is the photon energy;  $\sigma_{\gamma \rightarrow e^+e^-}$  is the Bethe-Heitler cross-section<sup>36</sup> for pair production;  $\langle \rho L \rangle_\Omega$  is the angle-averaged effective areal density for x-rays in the target;  $N_\gamma(k)$  is the  $\gamma$ -ray distribution created by the laser-produced relativistic electrons. The bremsstrahlung spectrum is given by:

$$N_\gamma(k) dk = \eta N_e \int_0^\infty dT_e f_0(T_e) \int_0^s ds' n_i \sigma_\gamma[E(E_0, s'), k] dk,$$

where  $f_0(T_e, E_0)$  is the (kinetic) energy spectrum of electrons created in the laser-target interaction that enter the solid target (of total number  $N_e$ ) with temperature  $T_e$  (given by ponderomotive or Puhkov's scaling),  $s'$  is a path-length variable for electrons of initial (final) energy  $E_0$  ( $s'=0$ ), such that their energy at  $s=s'$  [ $E(E_0, s')$ ] is calculated with the stopping power including the radiation loss,  $n_i$  is the ion density,  $\sigma_i$  is the relativistic radiation cross-section of bremsstrahlung,<sup>37</sup> and  $\eta$  is the “refluxing” parameter ( $0 < \eta < 1$ ), where  $\eta=1$  indicates the perfect refluxing until electrons lose energy and stop. The numerical integration of  $s'$  is done until the electron reaches  $s$  where it stops,  $E(s)=0$ . The calculated positron yield per kJ laser energy as a function of  $T_e$ , shown in Fig. 10, assumes 100% refluxing ( $\eta=1$ ). Although 100% refluxing is not possible, it is a reasonable approximation because only 0.1-1% of electrons are measured to escape the target.<sup>22</sup>

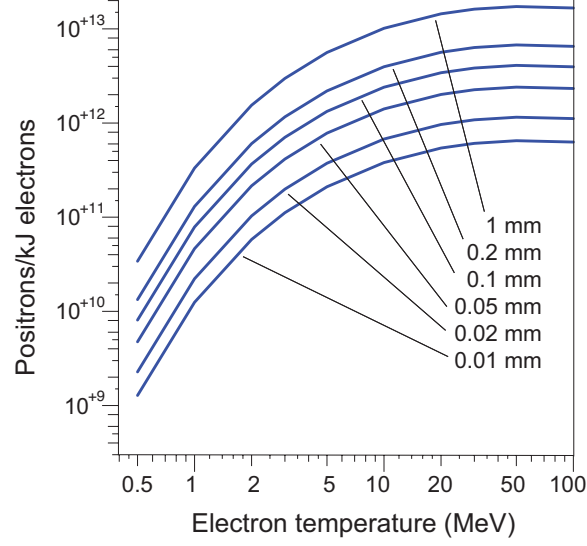


Figure 10: The semi-analytically calculated positron yield as a function of hot-electron temperature for gold targets of thickness ranging from 10  $\mu\text{m}$  to 1 mm.

(II) Using the particle transport code GEANT4, the pair production in a solid Au target was modeled in 3D. The laser-plasma interaction at the front surface of the target was not included. A total of  $3 \times 10^7$  randomly seeded electrons were initialized as a collimated, single-component Boltzmann distribution  $T_e$  in a uniform spot size with a radius of 10 microns. The actual target (gold disc of 2 mm diameter, 1 mm thick) was used in the model. The simulation box was 0.1 mm larger than the target dimensions. Electrons and positrons were subject to energy loss from bremsstrahlung, Coulomb scattering, and ionization events; positrons also annihilated with atomic electrons but no electromagnetic field effects are included. Photons above 1.5 keV were tracked and subject to photoelectric absorption, Compton scattering, and Bethe-Heitler pair production. Atomic relaxation due to fluorescence, Auger emission, and particle-induced x-ray emission were included in the simulation. Positrons born inside the target were recorded, and electrons, positrons, and photons escaping the target were counted at

the exterior of the simulation box. Positrons within a 1 sr solid angle of the back target surface normal were recorded.

The results from GEANT4 simulations as a function of  $T_e$  are shown in Fig. 11. Although the total number of positrons produced in the target as given by the GEANT4 and analytic calculation agree well at lower temperature ( $<5$  MeV), the discrepancy increases at higher temperatures due to the difference in their treatment of electron refluxing, as will be discussed further in the following sections.

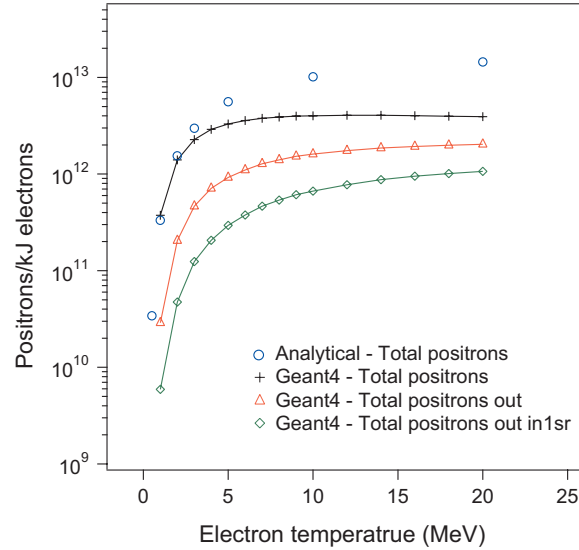


Figure 11: Three sets of Geant4 results of positron yield as a function of hot-electron temperature: the total number of positrons produced in the target (crosses); the total number of positrons emerging from the target (triangles); and the total number of positrons within 1 sr (diamonds). Also shown is the total positron production calculated using the analytical method (circles) as in Fig. 10.

The effect of transport through the target was quantified by taking the ratio between the total number of positrons produced inside the target, and the number that emerged from the target. This ratio provides an estimate of the total number of

observable positrons from the analytical calculation. Fig. 12 compares, as a function of  $T_e$ , the total number of positrons produced and emerging from the target given by GEANT4 and the analytic method. While these two methods give very similar positron yields at low electron temperatures, they deviate from each other by up to factor of 4 with increasing  $T_e$ . Based on the Particle-in-Cell simulations discussed in the next section, we believe that this is due to electron recirculation, which is not included in the GEANT4 simulation.

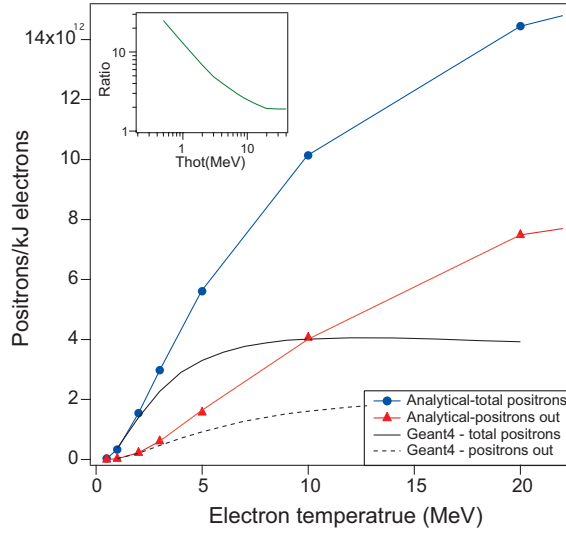


Figure 12: Positron yield per kJ of electrons, as a function of electron temperature. Inset: ratio between the total number of positrons produced inside the target (solid line) and the number emerging from the target (dotted line) calculated with GEANT4. This ratio is used to infer the total number positrons outside the target (triangles) from the values calculated inside the target by the analytical method (dots).

**(III)** Particle-In-Cell simulations were performed using the implicit hybrid code LSP in 2 stages: (1) a laser-plasma interaction with a 2D Cartesian high resolution simulation to model a 1 ps pulse duration with  $8 \times 10^{19} \text{ Wcm}^{-2}$  peak intensity laser incident

on a preformed plasma, and (2) a 2D RZ transport stage using the relativistic electron beam from the first simulation as a hot electron source. The electron source from the laser plasma simulation was increased in pulse duration by a factor of 10 to provide a surrogate for the Omega EP laser due to difficulties associated with modeling a 10 ps laser interaction. The transport simulation used a 2D axisymmetric geometry to more accurately represent the  $1/r^2$  falloff containing a 2 mm diameter, 1 mm thick solid Au target embedded in a vacuum box spanning 5 mm in radius and 1.5 cm in axial extent, as illustrated in Figure 13.

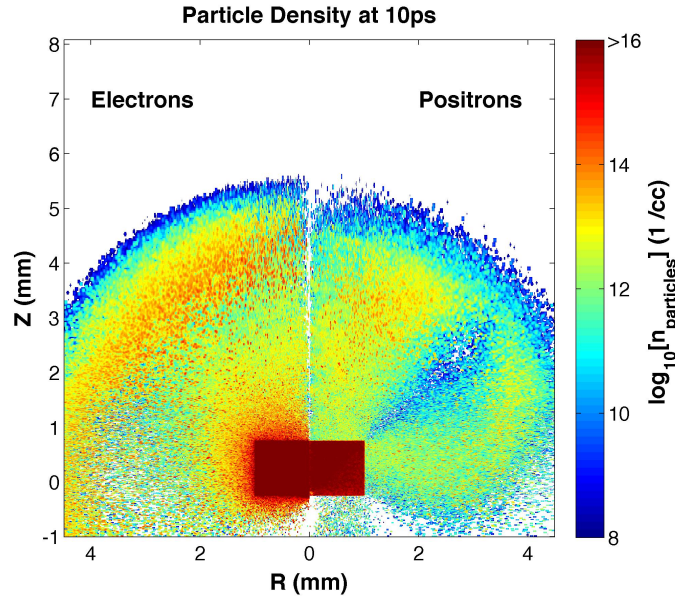


Figure 13: The electron and positron density in the LSP simulation at the time of peak electron beam intensity. A majority ( $> 90\%$ ) of the electrons and positrons are confined or stopped inside the gold target which extends from  $Z=-0.25-0.75$  mm and  $R \leq 1$  mm. Simulation boundaries extend far from the gold surface to include the effect of the sheath electric field on the escaping particle jets.

The solid Au target was modeled as a fluid starting at an initial temperature of 0.1 eV, using Lee-More-Desjarlais<sup>38</sup> conductivities to describe its collisional



properties. The hot electron source was injected into the Au target  $5\text{ }\mu\text{m}$  from the front surface containing  $550\text{ J}$  of electrons over a  $22\text{ ps}$  temporal duration (for a  $10\text{ ps}$  Gaussian pulse) with a time-integrated electron spectrum well described as a power law distribution with an exponent of  $-1.33$  for electrons below  $4\text{ MeV}$  and as 2 decaying exponentials ( $4.5$  and  $11.7\text{ MeV}$  with  $5:1$  ratio) above  $4\text{ MeV}$  out to  $120\text{ MeV}$ . Hot electron collisions were included through Atzeni-Schavi-Davies<sup>39</sup> stopping powers for the collisional heating of the gold, and photon generation was computed using the Integrated-TIGER-Series (ITS)<sup>40</sup> code. All photons emitted with energy above  $1\text{ keV}$  were transported in the simulation and their interactions with the gold modeled using ITS. Electron-positron pairs produced through the Bethe-Heitler mechanism were fed back into the simulation and self-consistently evolved. Simulations used a  $1\text{ fs}$  time step and ran for  $100\text{ ps}$  to capture the full refluxing dynamics and to model the modification of the escaping electron-positron plasma by self-generated fields. All escaping particles were recorded at a computational surrogate of the EPPS diagnostic, located  $1\text{ cm}$  from the initial Au target.

### **C. Positron yield: comparison between experiment and calculation**

Comparing the results of the three computational methods with the experimental data, a key finding is that the observed quadratic positron yield scaling with laser energy is the combined result of (a) the higher laser intensity achieved with higher laser energy when the focal spot and pulse duration are fixed, and (b) the additional electron-target interaction from enhanced electron refluxing due to the improved electrostatic confinement of the laser accelerated electrons.<sup>1</sup>

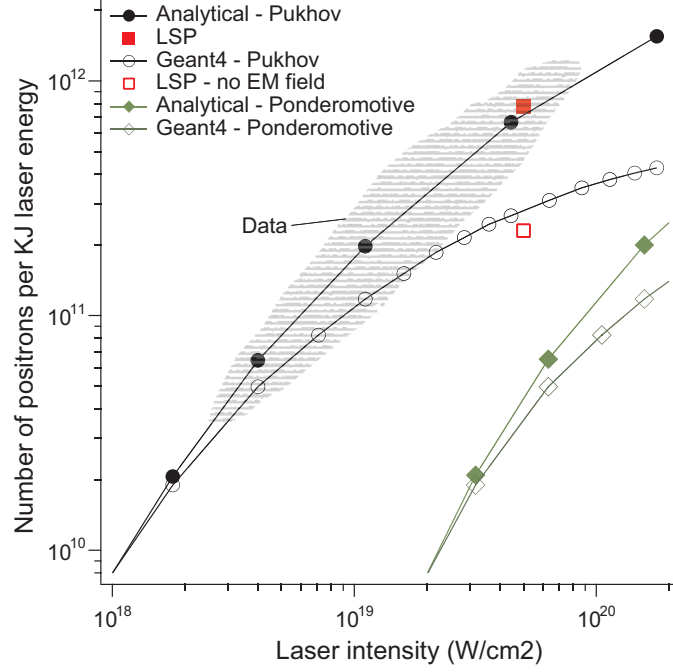


Figure 14: Positron yield per kJ laser energy as a function of laser intensity from analytical calculations including refluxing with Pukhov scaling of  $T_e$  (solid circles) or ponderomotive scaling of  $T_e$  (solid diamonds); GEANT4 simulations with Pukhov scaling (open circles) or ponderomotive scaling (open diamonds). The results from LSP simulations are shown either with refluxing (solid square) or without refluxing (open square). The shaded area covers the experimental data range.

Figure 14 shows that the analytic model and GEANT4 simulations using Pukhov scaling of  $T_e$  fit the data much better than using Ponderomotive scaling. Furthermore, the analytical calculation, which includes electron refluxing through the target, fits the data better than the GEANT4 results without it. The importance of the refluxing process is confirmed by the results of the self-consistent LSP particle-in-cell simulation shown as a solid red square (with refluxing) and a hollow square (without refluxing) in Fig. 14. Although this effect was previously identified in studies with thin targets,<sup>34</sup> it has not previously been realized for mm-thick targets at high intensities.

The agreement between the data and the positron yield calculated with refluxing confirms the important role of electron refluxing in the pair production, which results in positron yields about 4 times higher than those without refluxing at the highest laser energies and intensities reached in our experiments.

#### **D. Positron acceleration**

Acceleration away from the target in which the positrons are born, is a feature unique to positrons produced by direct laser-plasma interaction. Previous work reported<sup>17</sup> that such acceleration was caused by the well known target-normal electric field (sheath field) produced at the back of the target from the escaping electrons. This electric field is also responsible for the confinement/refluxing of hot electrons to the target, which enhances the positron yield compared to a single pass of the hot electrons through the target. The new experimental data presented here reinforces this conclusion.

The evidence that positrons are post-accelerated by the sheath field is clearly seen in Fig. 15: their energies at the peak of the distribution (red circles) are far higher than the “birth” peak energies calculated using GEANT4 simulations (black diamonds). The escaping positrons pick up 10 – 20 MeV in energy from the sheath-accelerating field. LSP simulations include this field self-consistently and their results agree with the measurement showing much increased positron peaks (green squares in Fig. 15).

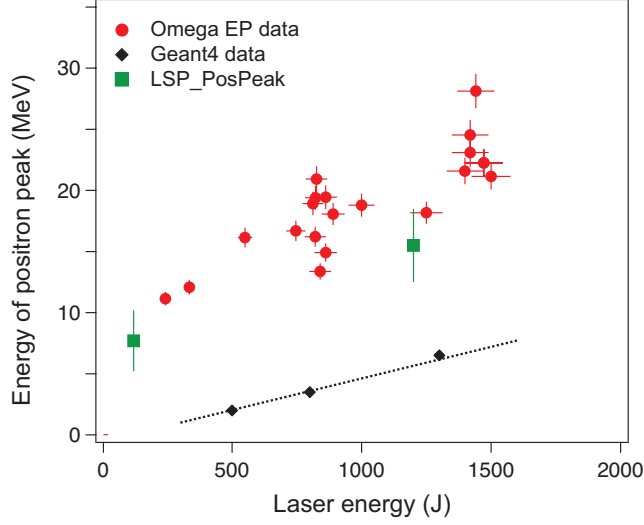


Figure 15: The energy corresponding to the peak of the positron distribution from measurements (red dots), LSP simulation (green squares) and from calculation (black diamonds) as a function of laser energy. The line is linear fit to the Geant4 data.

Figure 15 shows a linear dependence of positron peak energy vs laser energy  $E_L$ . This indicates a linear increase in sheath potential. The sheath electric field is established by the net charge left behind on the target as the most energetic electrons escape. The strength of this field is related to the total charge of these electrons and the capacitance of the target<sup>27</sup> as  $\epsilon_{sheath} \propto Q_e / C_{target}$ , where  $Q_e = eN_{esc}$ ,  $N_{esc}$  is the total number of escaping electrons, and  $C_{target}$  is determined by the target size. The data shown in Fig. 15 corresponds to a constant target size (capacitance), and  $N_{esc}$  increases linearly with incident laser energy as shown in Fig. 7, thus the expected  $\epsilon_{sheath}$  increases linearly with laser energy. This linear relationship is further illustrated in Fig. 16, which shows the measured positron peak energy as a function of  $N_{esc}$ . Independently, we have also verified experimentally that the positron peak energy depends linearly on  $1/C_{target}$  by increasing

the target diameter ( $C_{\text{target}}$  is proportional to the rear surface area of the target) while keeping the laser energy fixed.<sup>17</sup>

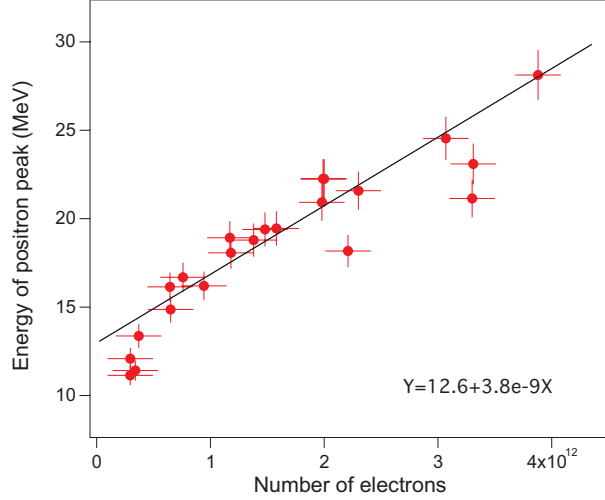


Figure 16: The measured energy of the peak in the positron distribution as a function of the total number of measured electrons. The line is the fit to the data for positron energy greater than 14 MeV.

Furthermore, the peak positron energy is found to correlate with the maximum proton energy measured on the same shot, as shown in Fig. 17. It is well established that the maximum energy of the protons produced at the rear surface of the target (via target normal sheath acceleration) is determined by the peak value of the sheath field.<sup>41</sup> Figure 17 demonstrates a linear relationship, with unity slope, between the positron peak energy and maximum proton energy, suggesting that the same physical mechanism – acceleration by the sheath field on the rear target surface – leads to both the positron and peak proton acceleration.

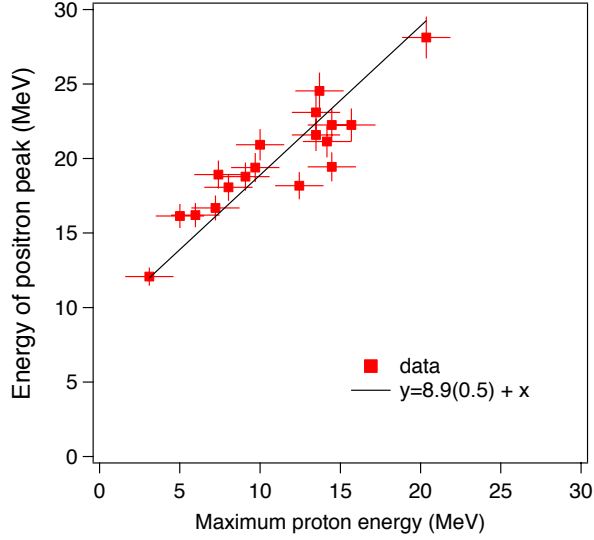


Figure 17: The energy of the peak in the positron distribution as a function of maximum proton energy measured from the same shots. The line has a slope of 1 and offset of 9 MeV.

### E Positron angular divergence

The angular distribution of the positrons has been shown to be jet-like<sup>17</sup>, which is further confirmed by the new data presented here. The data show that the divergence follows Liouville's theorem, and is therefore predictable. Liouville's theorem<sup>42</sup> implies that the emittance of the positron beam remains constant, despite any post-birth field acceleration. In other words, the transverse component of the positron momentum ( $m_{e^+}v_{\perp}$ ) remains constant, while the longitudinal momentum ( $m_{e^+}v_{\parallel}$ ) increases due the sheath electric field of the target. The emitted positron angular divergence is determined by the ratio of the transverse and longitudinal momenta, and as shown in Fig. 15 the peak positron energy and peak sheath electric field have a linear dependence on the incident laser energy. Since under these conditions the mean birth energy of positrons is much less than the energy gain from the sheath electric field, the divergence angle of the positron jet will then be proportional to  $E_L^{-1/2}$ , as shown by the red curve in Fig. 18. It should be noted that

at a laser energy of 10 kJ, where the positron yield is expected to reach astrophysical relevance, the divergence angle of the positron jet is expected to decrease to about  $5^\circ$ —near a pencil-like beam.

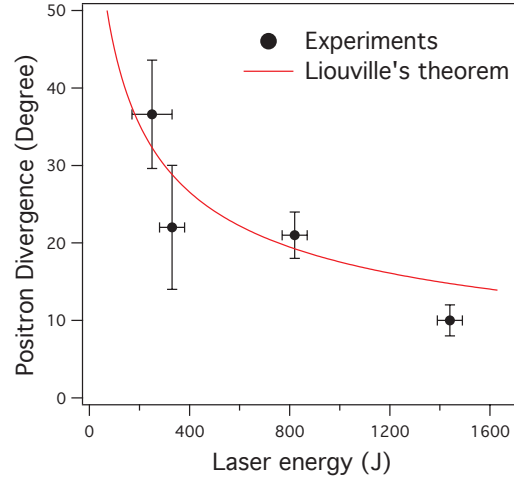


Figure 18: Positron divergence angle as a function of laser energy (dots with error bars). The behavior calculated from Liouville's theorem is shown by the red line.

#### F. Positron production rate, flux and energy conversion efficiency from laser

The positron production rate can be estimated as the ratio of the total number of positrons and the positron pulse duration. While the former is measured, the later is assumed to be the laser pulse duration. Experimentally it is difficult to measure charged particle phenomena in the picosecond regime, due to the lack of sufficiently fast charge-sensitive detectors. However, the validity of the assumption is confirmed by the 2D LSP simulations, as illustrated in Fig. 19. Given the laser pulse duration of 6.35 ps, the positron pulse duration is calculated to be about 7.4 ps at FWHM, an increase of only 16%.

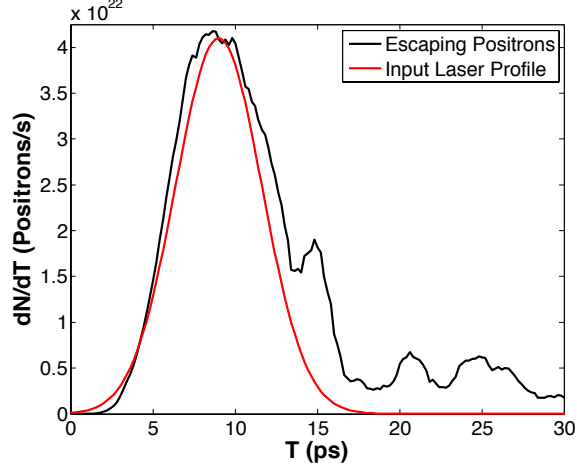


Figure 19: Escaping positron rate and input laser pulse as a function of time calculated from LSP simulation.

Table 2 summarizes the characteristics of the laser-produced positrons deduced from experimental information reported here. The positron source size used to calculate the peak flux is taken from reference.<sup>19</sup>

Table 2: Parameters of laser produced positron beams

Positron number	$10^{10} - 10^{12}$
Peak energy/positron acceleration	4 - 30 MeV
Beam divergence	45 – 15 deg
Flux duration	~1-20 ps
Energy conversion from laser pulse	$> 1 \times 10^{-4}$
Pair production rate	$\sim 10^{22} / \text{s}$
Peak flux	$> 10^{25} \text{ cm}^{-2} \text{ s}^{-1}$

## V. Comparison of current laboratory pair jet conditions to those needed for astrophysically-relevant experiments

The requirements for studying astrophysically-relevant phenomena using laboratory produced electron-positron jets have been previously discussed.<sup>1</sup> Here we give only a



brief summary. To use colliding laboratory pair jets to study the development of the Weibel instability and the magnetic field dynamics associated with relativistic collisionless shocks, the duration of the pair jets needs to be greater than the typical time ( $\tau_0 = 1/\Gamma = \gamma_0 * \sqrt{2}\omega_{pe}$ ) for instability growth, where  $\Gamma$  is the instability growth rate and  $\omega_{pe}$  the electron plasma frequency. This condition can be rewritten in terms of the minimum number of pairs that need to be produced to study the Weibel instability as  $N > 1.5 \times 10^{11} (R_0) 2\gamma_0 / \tau_0$  [ps], where  $R_0$  is the radius (in mm) and  $\gamma_0$  the relativistic factor of the electron-positron jets. This estimate sets a limit for a laboratory system to be useful to study relativistic driven by the relativistic pairs of relevance to astrophysical environments. Quantitatively, for a 10 ps long, ~mm-scale flow at ~ MeV energy, the required pair yield is  $>10^{11}$ . Likewise, for a 0.1 ps long, ~mm-scale flow, the pair yield needs to be  $>10^{13}$ .

Table 3 lists the parameters presently achieved in pair jet experiments in the context of values desired for astrophysically relevant experiments. While jets of sufficient temperature and duration have been produced, present experiments have not yet produced sufficiently dense beam of positrons to achieve a near-unity ratio between the densities of electrons and positrons. The primary goal for future research is to increase the positron density, thus establishing a viable experimental platform for using laser-produced pair jets in astrophysical applications.

*Table 3: Parameters of laser produced electron-positron jets relative to those needed for laboratory astrophysics experiments. The principal shortfall is highlighted in bold.*

Parameter	Current Experimental Range	Desired for Astrophysics Relevant Experiments
$T_{\parallel}$	0.5 - 4 MeV	$\sim$ MeV
$T_{\perp}$	0.2-1 MeV	$\sim$ MeV
$n_{e+}$	<b><math>\sim 10^{11-13} \text{ cm}^{-3}</math></b>	$> 10^{14-16} \text{ cm}^{-3}$
$n_{e-}$	$\sim 10^{12-15} \text{ cm}^{-3}$	$> 10^{14-16} \text{ cm}^{-3}$
$\tau_{\text{jet}}$	5 – 20 ps	$> 10$ ps

## VI. Future research

To bring the currently available laser-produced pair jet conditions closer to those needed for laboratory astrophysics experiments, the following approaches may be taken:

(A). Increase the pair numbers using more powerful lasers. It is easily deduced from the energy scaling of the pairs and the parameters summarized in Table 3 that astrophysically relevant pair jets could be produced using an order of magnitude larger laser energy. Such a laser would produce about 100 times more positrons and 10 times more electrons than current facilities, and these higher yields would be comparable to those needed for laboratory astrophysics experiments. And in fact, a new generation of intense high energy lasers, including NIF ARC,<sup>43</sup> Gekko LFEX<sup>44</sup> and LMJ PETAL,<sup>45</sup> are being constructed to deliver about 10 kJ at 1-10 ps pulse durations. These are expected to be available for experiments in the next few years. Figure 20 illustrates how NIF-ARC, for example, is expected to extend the available parameter space in density and duration. Fig. 20 shows that for currently achievable electron positron yields ( $\sim 10^{12}$ ) such as those from Omega EP lasers, it starts to be possible to study the linear phase of the instability

and observe the conversion of the kinetic energy of the flows into magnetic energy. By increasing the laser energy to 10-20 kJ, for which the yield is expected to be about  $10^{14}$ , it will be possible to study the saturation of the instability and the formation of a shock.<sup>1</sup>

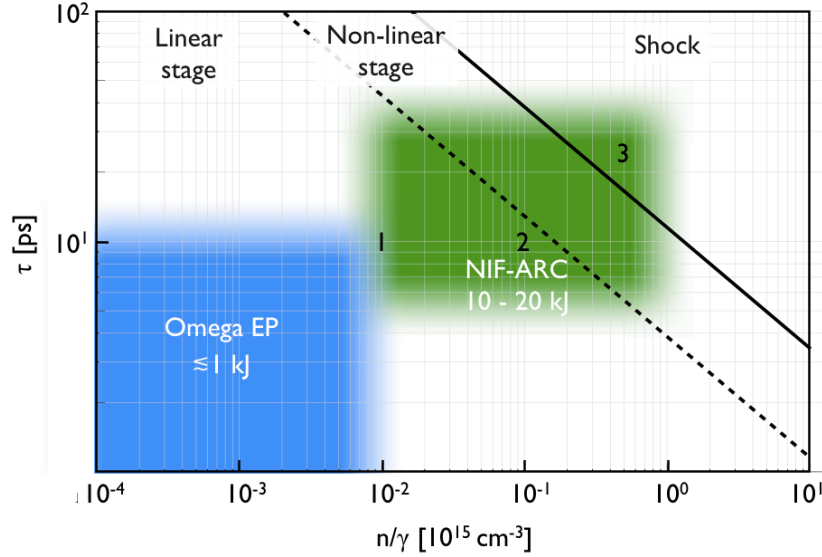


Figure 20. Pair plasma conditions required to study the different phases of formation of relativistic shocks in counter-streaming flows. Points 1, 2, and 3 correspond respectively to the necessary conditions for observing linear instability growth, saturated instability growth, and shock formation.<sup>1</sup> The black lines highlight the theoretical expectations for the saturation of the Weibel instability (dashed) and for shock formation (black).

(B). Develop magnetic collimation of the relativistic pair jets to increase the density in a larger volume. At present, although very high positron and electron densities are achieved near the back of the target, in the absence of collimation the pair density rapidly declines as the jet propagates away from the target. To maintain the high pair density achieved over a longer propagation distance (larger volume), it is important to pursue the development of magnetic fields to collimate and focus the pair jets. The

effectiveness of magnetic collimation has been demonstrated in experiments at Omega EP, in which a relativistic pair jet with  $\sim 15$  MeV peak energy was collimated using magnetic fields from an external, pulsed Helmholtz-type coil.<sup>18</sup> The collimation leads to a “pencil-like” positron beam with an equivalent FWHM (full width at half maximum) divergence angle of  $4^\circ$  vs the un-collimated beam with divergence of about  $20^\circ$ . A fraction of the laser-produced relativistic electrons with energies close to those of the positrons is also collimated, so that the ratio ( $n_e/n_{e+}$ ) in the co-propagating electron-positron jet is reduced from  $\sim 100$  (no collimation) to  $\sim 2.5$  with collimation. The positron density in the collimated beam increased from  $5 \times 10^7 \text{ cm}^{-3}$  to  $1.9 \times 10^9 \text{ cm}^{-3}$ . More importantly, such density was maintained for a distance of 0.5 meters, creating a sufficiently large plasma column for the study of pair-jet interactions. However, to collimate higher energy pairs, one would need magnetic field strengths higher than 10s of Tesla. Options for achieving this include laser produced magnetic fields.<sup>46,47</sup>

(C). Develop relativistic pair plasma confinement. While unconfined dense pair jets are expected to be very useful for laboratory astrophysics (to initiate instability growth through jet-jet, or jet-plasma interactions), it is important to have the pair plasma confined for studies of phenomena that take longer than 10s ps to develop, such as magnetic reconnection. To capture and confine relativistic pair jets, the magnetic “mirror” geometry, established over decades of magnetic confinement fusion research,<sup>48</sup> may be used. Relative to conditions in magnetic fusion plasmas, as well as low temperature/energy single component positron plasmas,<sup>49</sup> the key features of confined relativistic pair plasmas are very short time scales (sub nano-second), relativistic energies ( $> \text{MeV}$ ) and densities up to 2 orders of magnitude greater than in conventional

magnetically confined fusion plasmas. However, with the rapid development of transient high magnetic field generators using lasers and pulsed-power devices, mirror-confined relativistic pair plasmas may be realized in the laboratory in the near future.

In summary, this work reports new experimental results from three large laser facilities that reveal the energy scaling of both electrons and positrons from intense lasers interacting with mm-scale gold targets. The physics behind the scaling of laser-produced positrons was discovered to involve the combination of higher energy electrons from acceleration in underdense plasma, and the unexpected electron refluxing in mm-thick targets. The latter process was revealed by experimental evidence for the acceleration of positrons by the sheath electric field of the target, established by correlating positron data with those for the electrons and protons. In addition, the scaling of the angular divergence of positrons with laser energy is found to follow Liouville's theorem. Finally, a set of simultaneously achievable pair-plasma parameters was derived from the experimental data, compared with those needed for laboratory astrophysics experiments, and used to inform directions for future research.

Acknowledgement: Acknowledgement: We acknowledge the support of the Omega EP, Titan and Orion laser facilities for the experiments. HC thanks Peter Beiersdorfer, Bob Cauble, Henry Shaw and Bill Goldstein for encouragement and support. HC also thanks Laurent Divol and Nino Landen for discussion. This work was performed under the auspices of the U.S. DOE by LLNL under Contract DE-AC52-07NA27344, and partially funded by the LDRD (12-ERD-062) program.

## VII. Appendix – Notes on the measured electron spectra

The following three notes provide additional information and observations relevant to the electron energy distribution measurements and data analysis in various experiments, not limited to those described in this paper.

### 1). Electron energy distribution

Electron spectra often have detailed features that are difficult to describe with, for example, an exponential energy distribution, or for that matter any other distribution decreasing monotonically with particle energy. For example, Fig. 21 shows four spectra, three of which have “inverted distribution” features between about 2-10 MeV that cannot be fitted with a conventional hot electron temperature. Because of this, and considering that pair production is mostly driven by high-energy electrons, the spectra discussed in this work were fit only from 5 MeV and above to deduce the effective electron temperature.

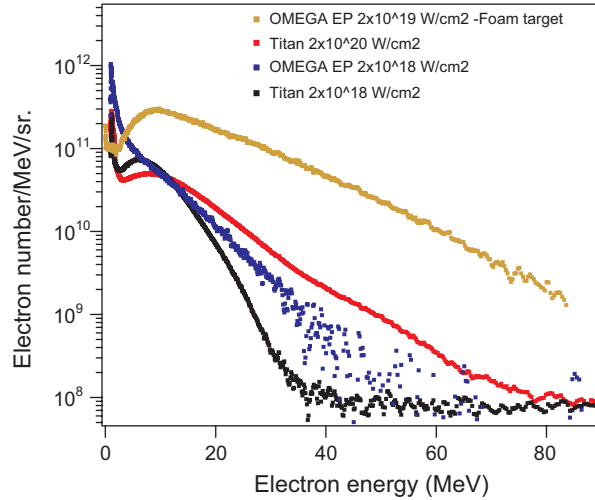


Figure: 21: Electron spectra from four shots at two facilities, with laser intensity of  $10^{18} - 10^{20}$  W/cm<sup>2</sup>.

## 2). Electron distribution as a function of preformed plasma

The electron energy distribution depends strongly on the laser interaction with the preformed plasmas – a feature that has been extensively studied theoretically [Ref 31 and references cited therein] and experimentally.<sup>50</sup> It is also seen in our measurements. Figure 22 shows the spectra taken at the Titan laser from three shots with a deliberately added prepulse. The intrinsic prepulse level is about 50 mJ contained in a 1-3 ns laser pedestal. The bottom two electron spectra represent the shot-to-shot uncertainty due to the uncontrollable prepulse: the additional 10-40 mJ prepulse on top of the intrinsic prepulse is not significant enough to cause any effect in the electron temperature. However, the deliberate injection of another 840 mJ of prepulse significantly increases the resulting electron temperature ( $\sim 16$  MeV).

An alternative way to describe the prepulse effect on the hot tail of the electron distribution is shown, using a separate set of data, in Fig. 23, where the number of electrons was binned on a very coarse energy grid. An increase in the prepulse energy corresponds to a decrease of electrons in the low energy bin and a corresponding increase in the high-energy bin. Larger prepulse injection effectively results in a larger fraction of outgoing electrons at higher energy.

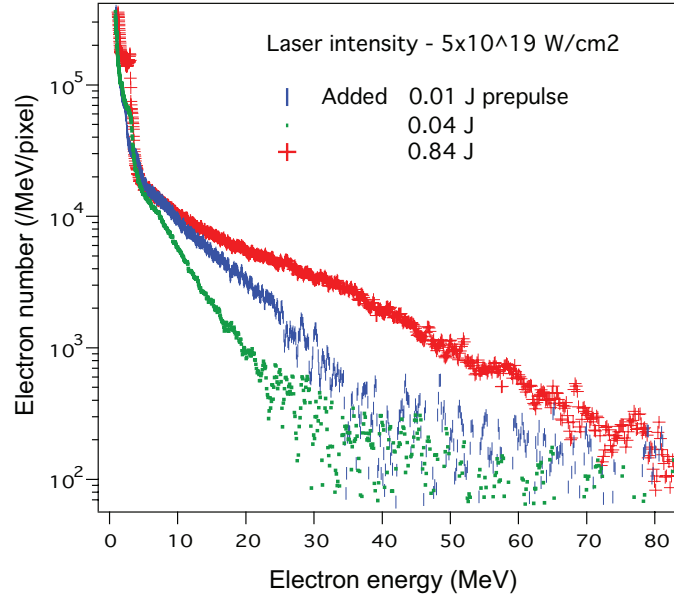


Figure: 22. Electron spectra with pre-pulse injection energy of 10 (blue bars), 40 (green dots) and 840 mJ (red crosses), with corresponding hot electron temperatures of 8, 5 and 16 MeV, respectively.

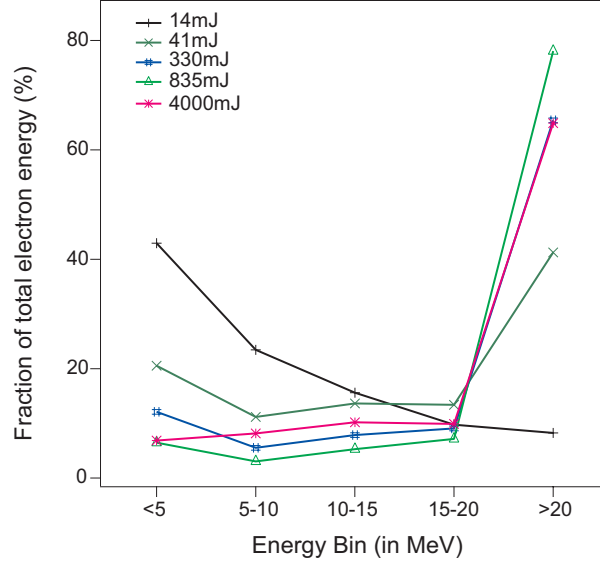


Figure: 23: Fraction of outgoing electron energy for shots with different pre-pulse injection energy (10 to 4000 mJ) measured in various energy bins.



### 3). Electron distribution as a function of target size

The data obtained in the experiments described in this paper indicate that the hot electron temperature depends at most weakly on the target size and thickness. Figure 24a shows the measured electron distributions taken from Titan experiments at about  $5 \times 10^{19}$  W/cm<sup>2</sup> where the targets were square, 12  $\mu$ m thick silver foils of various sizes. The data show that the electron temperatures derived from electrons with energies greater than 5 MeV are insensitive to the target size (i.e. at the high electron energies the slopes are similar). Similar conclusions are found in the spectra taken from 1 mm thick gold targets of various sizes as shown in Fig. 24b. On the other hand, the number of hot electrons escaping the target increases with increasing target size, because the sheath potential decreases as the capacitance of the target increases<sup>22</sup> (see Sec. IV-D).

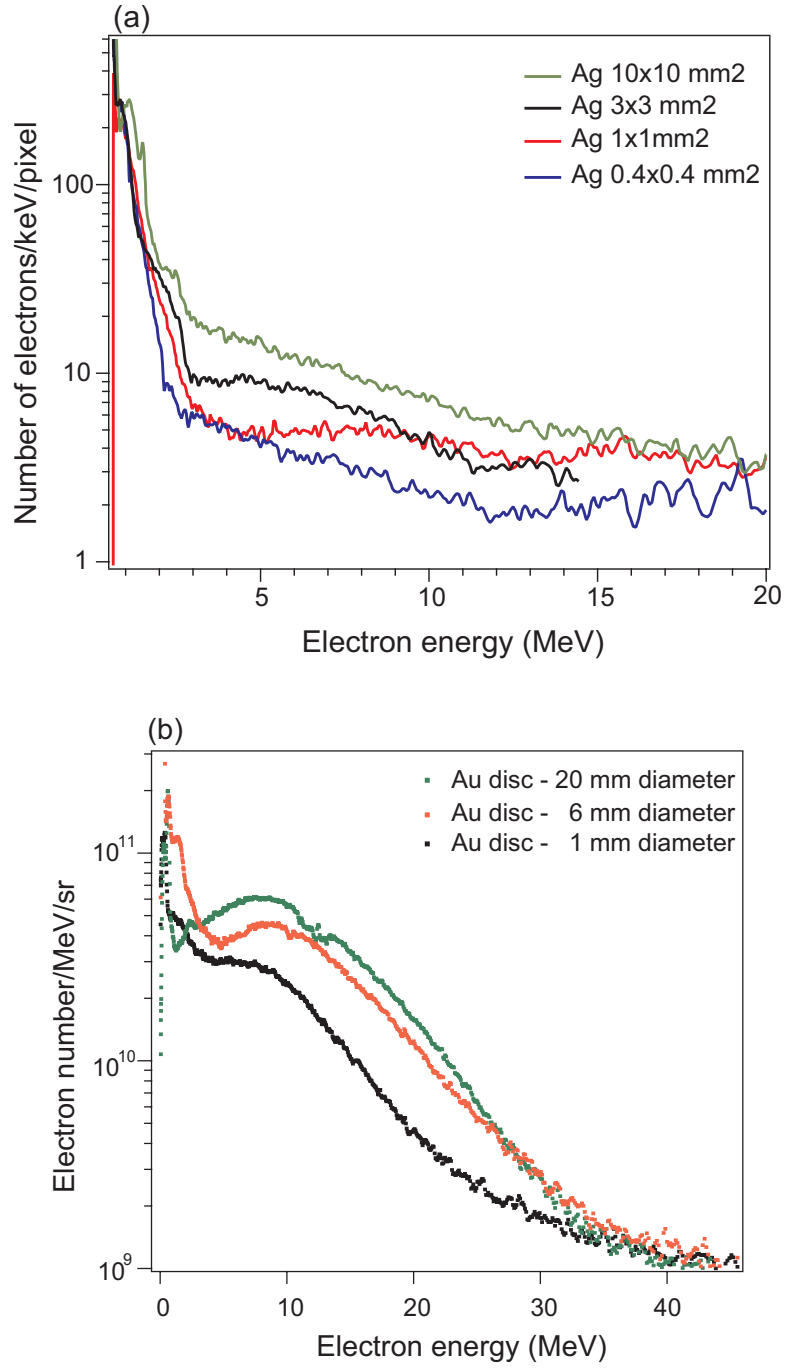


Figure: 24: Effect of target size on the hot electron spectra for (a) Ag targets and (b) Au targets.

Reference:

- <sup>1</sup> H. Chen, F. Fuiza, A. Hazi, M. Hill, D. Hoarty, S. James, S. Kerr, A. Link, D.D. Meyerhofer, J. Myatt, Y. Sentoku, and G.J. Williams, Submitted to Phys. Rev. Lett. (2015).
- <sup>2</sup> B. A. Remington, Science (80-. ). **284**, 1488 (1999).
- <sup>3</sup> B. Paczynski, Astrophys. J. **308**, L43 (1986).
- <sup>4</sup> M.J. Rees and P. Meszaros, Mon. Not. R. Astron. Soc. **258**, 41P (1992).
- <sup>5</sup> T. Piran, Rev. Mod. Phys. **76**, 1143 (2005).
- <sup>6</sup> P. Mészáros, Reports Prog. Phys. **69**, 2259 (2006).
- <sup>7</sup> E. Waxman, Phys. Rev. Lett. **75**, 386 (1995).
- <sup>8</sup> T. Piran, Phys. Rep. **314**, (1999).
- <sup>9</sup> H. Chen, S. Wilks, J. Bonlie, E. Liang, J. Myatt, D. Price, D. Meyerhofer, and P. Beiersdorfer, Phys. Rev. Lett. **102**, 1 (2009).
- <sup>10</sup> H. Chen, D.D. Meyerhofer, S.C. Wilks, R. Cauble, F. Dollar, K. Falk, G. Gregori, A. Hazi, E.I. Moses, C.D. Murphy, J. Myatt, J. Park, J. Seely, R. Shepherd, A. Spitkovsky, C. Stoeckl, C.I. Szabo, R. Tommasini, C. Zulick, and P. Beiersdorfer, High Energy Density Phys. **7**, 225 (2011).
- <sup>11</sup> E. Weibel, Phys. Rev. Lett. **2**, 83 (1959).
- <sup>12</sup> ATHENA Collaboration, Nature **419**, 456 (2002).
- <sup>13</sup> G. Gabrielse, N.S. Bowden, P. Oxley, a Speck, C.H. Storry, J.N. Tan, M. Wessels, D. Grzonka, W. Oelert, G. Schepers, T. Sefzick, J. Walz, H. Pittner, T.W. Hänsch, and E. a Hessels, Phys. Rev. Lett. **89**, 213401 (2002).
- <sup>14</sup> P.M. Platzman and A.P. Mills, Phys. Rev. B **49**, 454 (1994).
- <sup>15</sup> A.P. Mills, Nucl. Instruments Methods Phys. Res. Sect. B Beam Interact. with Mater. Atoms **192**, 107 (2002).
- <sup>16</sup> T.E. Cowan, M.D. Perry, M.H. Key, T.R. Ditmire, S.P. Hatchett, E. a. Henry, J.D. Moody, M.J. Moran, D.M. Pennington, T.W. Phillips, T.C. Sangster, J. a. Sefcik, M.S. Singh, R. a. Snavely, M. a. Stoyer, S.C. Wilks, P.E. Young, Y. Takahashi, B. Dong, W. Fountain, T. Parnell, J. Johnson, a. W. Hunt, and T. Kühl, Laser Part. Beams **17**, 773 (1999).
- <sup>17</sup> H. Chen, S. Wilks, D. Meyerhofer, J. Bonlie, C. Chen, S. Chen, C. Courtois, L. Elbertson, G. Gregori, W. Kruer, O. Landoas, J. Mithen, J. Myatt, C. Murphy, P. Nilson, D. Price, M. Schneider, R. Shepherd, C. Stoeckl, M. Tabak, R. Tommasini, and P. Beiersdorfer, Phys. Rev. Lett. **105**, 1 (2010).
- <sup>18</sup> H. Chen, G. Fiksel, D. Barnak, P.-Y. Chang, R.F. Heeter, a. Link, and D.D. Meyerhofer, Phys. Plasmas **21**, 040703 (2014).

- <sup>19</sup> H. Chen, J.C. Sheppard, D.D. Meyerhofer, a. Hazi, a. Link, S. Anderson, H. a. Baldis, R. Fedosejev, J. Gronberg, N. Izumi, S. Kerr, E. Marley, J. Park, R. Tommasini, S. Wilks, and G.J. Williams, *Phys. Plasmas* **20**, 013111 (2013).
- <sup>20</sup> W. Heitler, *The Quantum Theory of Radiation* (Clarendon Press, Oxford, 1954).
- <sup>21</sup> W. Leemans and E. Esarey, *Phys. Today* **62**, 44 (2009).
- <sup>22</sup> B.C. Stuart, J.D. Bonlie, J.A. Britten, J.A. Caird, R. Cross, C.A. Ebberts, M.J. Eckart, A.C. Erlandson, W.A. Molander, A. Ng, P.K. Patel, and D.F. Price, in *Conf. Lasers Electro-Optics/Quantum Electron. Laser Sci. Conf. Photonic Appl. Syst. Technol.* (Optical Society of America, Long Beach, California, 2006), p. JTuG3.
- <sup>23</sup> L.J. Waxer, D.N. Maywar, J.H. Kelly, T.J. Kessler, B.E. Kruschwitz, S.J. Loucks, R.L. McCrory, D.D. Meyerhofer, S.F.B. Morse, C. Stoeckl, and J.D. Zuegel, *Opt. Photonics News* **16**, 30 (2005).
- <sup>24</sup> N. Hopps, C. Danson, S. Duffield, D. Egan, S. Elsmere, M. Girling, E. Harvey, D. Hillier, M. Norman, S. Parker, P. Treadwell, D. Winter, and T. Bett, *Appl. Opt.* **52**, 3597 (2013).
- <sup>25</sup> H. Chen, A.J. Link, R. van Maren, P.K. Patel, R. Shepherd, S.C. Wilks, and P. Beiersdorfer, *Rev. Sci. Instrum.* **79**, 10E533 (2008).
- <sup>26</sup> H. Chen, R. Tommasini, J. Seely, C.I. Szabo, U. Feldman, N. Pereira, G. Gregori, K. Falk, J. Mithen, and C.D. Murphy, *Rev. Sci. Instrum.* **83**, 2012 (2012).
- <sup>27</sup> A. Link, R.R. Freeman, D.W. Schumacher, and L.D. Van Woerkom, *Phys. Plasmas* **18**, 053107 (2011).
- <sup>28</sup> B.I. Cohen, A.J. Kemp, and L. Divol, *J. Comput. Phys.* **229**, 4591 (2010).
- <sup>29</sup> S. Wilks, W. Kruer, M. Tabak, and A. Langdon, *Phys. Rev. Lett.* **69**, 1383 (1992).
- <sup>30</sup> A. Pukhov, Z.-M. Sheng, and J. Meyer-ter-Vehn, *Phys. Plasmas* **6**, 2847 (1999).
- <sup>31</sup> A.J. Kemp, F. Fiuza, A. Debayle, T. Johzaki, W.B. Mori, P.K. Patel, Y. Sentoku, and L.O. Silva, *Nucl. Fusion* **54**, 054002 (2014).
- <sup>32</sup> Y. Ping, R. Shepherd, B. Lasinski, M. Tabak, H. Chen, H. Chung, K. Fournier, S. Hansen, A. Kemp, D. Liedahl, K. Widmann, S. Wilks, W. Rozmus, and M. Sherlock, *Phys. Rev. Lett.* **100**, 085004 (2008).
- <sup>33</sup> P. Gibbon, *Short pulse laser interactions with matter*, Imperial College Press, 2005.
- <sup>34</sup> P.M. Nilson, J.R. Davies, W. Theobald, P. a. Jaanimagi, C. Mileham, R.K. Jungquist, C. Stoeckl, I. a. Begishev, a. a. Solodov, J.F. Myatt, J.D. Zuegel, T.C. Sangster, R. Betti, and D.D. Meyerhofer, *Phys. Rev. Lett.* **108**, 085002 (2012).
- <sup>35</sup> J. Myatt, J. Delettrez, A. Maximov, D. Meyerhofer, R. Short, C. Stoeckl, and M. Storm, *Phys. Rev. E* **79**, 066409 (2009).
- <sup>36</sup> J.H. Hubbell, H.A. Gimm, and I. Overbo, *J. Phys. Chem. Ref. Data* **9**, 1023 (1980).
- <sup>37</sup> J.D. Jackson, *Classical Electrodynamics* (Wiley, 1998).
- <sup>38</sup> M. Desjarlais, *Contrib. to Plasma Phys.* **41**, 2 (2001).

- <sup>39</sup> S. Atzeni, A. Schiavi, and J.R. Davies, *Plasma Phys. Control. Fusion* **51**, 015016 (2009).
- <sup>40</sup> J. Halbleib, R.P. Kensek, S.M. Seltzer, and M.J. Berger, **39**, 1025 (1992).
- <sup>41</sup> A. Mackinnon, M. Borghesi, S. Hatchett, M. Key, P. Patel, H. Campbell, A. Schiavi, R. Snively, S. Wilks, and O. Willi, *Phys. Rev. Lett.* **86**, 1769 (2001).
- <sup>42</sup> M. Conte and W.W. MacKay, *An Introduction to the Physics of Particle Accelerators*, World Scientific, New Jersey, second edition, 2008
- <sup>43</sup> J.K. Crane, G. Tietbohl, P. Arnold, E.S. Bliss, C. Boley, G. Britten, G. Brunton, W. Clark, J.W. Dawson, S. Fochs, R. Hackel, C. Haefner, J. Halpin, J. Heebner, M. Henesian, M. Hermann, J. Hernandez, V. Kanz, B. McHale, J.B. McLeod, H. Nguyen, H. Phan, M. Rushford, B. Shaw, M. Shverdin, R. Sigurdsson, R. Speck, C. Stolz, D. Trummer, J. Wolfe, J.N. Wong, G.C. Siders, and C.P.J. Barty, *J. Phys. Conf. Ser.* **244**, 032003 (2010).
- <sup>44</sup> H. Shiraga, S. Fujioka, M. Nakai, T. Watari, H. Nakamura, Y. Arikawa, H. Hosoda, T. Nagai, M. Koga, H. Kikuchi, Y. Ishii, T. Sogo, K. Shigemori, H. Nishimura, Z. Zhang, M. Tanabe, S. Ohira, Y. Fujii, T. Namimoto, Y. Sakawa, O. Maegawa, T. Ozaki, K. Tanaka, H. Habara, T. Iwawaki, K. Shimada, H. Nagatomo, T. Johzaki, a Sunahara, M. Murakami, H. Sakagami, T. Taguchi, T. Norimatsu, H. Homma, Y. Fujimoto, a Iwamoto, N. Miyanaga, J. Kawanaka, T. Jitsuno, Y. Nakata, K. Tsubakimoto, N. Morio, T. Kawasaki, K. Sawai, K. Tsuji, H. Murakami, T. Kanabe, K. Kondo, N. Sarukura, T. Shimizu, K. Mima, and H. Azechi, *Plasma Phys. Control. Fusion* **53**, 124029 (2011).
- <sup>45</sup> D. Batani, M. Koenig, J.L. Miquel, J.E. Ducret, E. d’Humieres, S. Hulin, J. Caron, J.L. Feugeas, P. Nicolai, V. Tikhonchuk, L. Serani, N. Blanchot, D. Raffestin, I. Thfoin-Lantuejoul, B. Rosse, C. Reverdin, a Duval, F. Laniesse, a Chancé, D. Dubreuil, B. Gastineau, J.C. Guillard, F. Harrault, D. Leboeuf, J.-M. Le Ster, C. Pès, J.-C. Toussaint, X. Leboeuf, L. Lecherbourg, C.I. Szabo, J.-L. Dubois, and F. Lubrano-Lavaderci, *Phys. Scr.* **T161**, 014016 (2014).
- <sup>46</sup> M. Tatarakis, I. Watts, F.N. Beg, E.L. Clark, a E. Dangor, a Gopal, M.G. Haines, P. a Norreys, U. Wagner, M.-S. Wei, M. Zepf, and K. Krushelnick, *Nature* **415**, 280 (2002).
- <sup>47</sup> S. Fujioka, Z. Zhang, K. Ishihara, K. Shigemori, Y. Hironaka, T. Johzaki, A. Sunahara, N. Yamamoto, H. Nakashima, T. Watanabe, H. Shiraga, H. Nishimura, and H. Azechi, *Sci. Rep.* **3**, 1170 (2013).
- <sup>48</sup> J. Wesson, *Tokamaks*, 4th ed. (Oxford University Press, 2011).
- <sup>49</sup> C.M. Surko and R.G. Greaves, *Phys. Plasmas* **11**, 2333 (2004).
- <sup>50</sup> T. Yabuuchi, B.S. Paradkar, M.S. Wei, J. King, F.N. Beg, R.B. Stephens, N. Nakanii, M. Hatakeyama, H. Habara, K. Mima, K. Tanaka, and J.T. Larsen, *Phys. Plasmas* **17**, 12 (2010).